

# Multi-passage time-resolved CFD analysis of rotor tip stall inception and passive control in a highly-loaded axial compressor

## M. Kawase

PhD Student, Department of Engineering  
University of Leicester  
Leicester, UK

## A. Rona

Associate Professor, Department of Engineering  
University of Leicester  
Leicester, UK

## ABSTRACT

Tip stall inception in a high speed jet axial rotor, if induced at a critical phase in a sortie, can compromise the stability of the engine and undermine the aircraft safety. Steady and time-resolved Computational Fluid Dynamics (CFD) is used to investigate the flow through a highly loaded axial rotor, at a stage pressure ratio representative of future highly manoeuvrable combat aircraft systems. The base flow from which tip stall onsets and the early stages of tip stall are modelled, reproducing the salient stages of the flow processes leading to an axial compressor rotating stall, by flow separation at the rotor tip. A casing treatment concept aimed at mitigating this stall type is explored by CFD. The treatment features a channel that provides passive flow control by flow recirculation. Some novel design aspects of the channel geometry are considered. A numerical investigation of the channel parameter space, by varying the axial length, achieved a 9.11% improvement in the compressor stall margin with respect to the baseline CFD prediction, without any adiabatic efficiency penalty. The time-dependent CFD simulations provided some useful insights on the stall inception process in the highly loaded axial compressor with the recirculation channel treatment.

## NOMENCLATURE

CFD Computational Fluid Dynamics  
MCA Multiple-Circular-Arc

### Symbols

$c_p$  Specific heat capacity at constant pressure  
 $c_t$  Pressure resistance coefficient  
 $c_z$  Axial chord length  
 $e$  Relative error  
 $h_r$  Radial height from the hub  
 $H_r$  Radial height from the hub to the casing  
 $I$  Turbulence intensity

$k$  Specific turbulent kinetic energy  
 $l$  Turbulence length scale  
 $\dot{m}$  Mass flow rate  
 $P$  Pressure  
 $r_m$  Refinement ratio  
 $T$  Temperature  
 $t_{rev}$  Time in rotor revolutions  
 $U_{tip}$  Rotor speed at the tip, 454.1 m s<sup>-1</sup>  
 $u_a$  Axial velocity  
 $u_t$  Tangential velocity  
 $y^+$  Near-wall resolution  
 $\gamma$  Specific heat ratio, 1.4  
 $\epsilon$  Specific dissipation rate of specific turbulent kinetic energy  
 $\eta$  Adiabatic efficiency  
 $\rho$  Density  
 $\omega_3$  Rotational speed

### Subscripts

0 Stagnation condition  
1 Station 1  
4 Station 4  
in Computational domain inlet  
n Mesh index  
out Computational domain outlet  
R Richardson's extrapolation  
ref Reference

### Superscripts

$\bar{\phantom{x}}$  Mass-averaging

## 1.0 INTRODUCTION

Providing a stable operation is one of the essential requirements for aircraft engines to ensure a safe flights. Since the engine is a significant contribution to the aircraft weight, engine weight reduction has been one of the most significant topics for designers to decrease the fuel consumption through all the flight phases. This has progressively increased the thrust-to-weight ratio of fighter aircraft engines. The axial compressor is critical to the stability performance of fast jet engines. Contributing to the aircraft weight reduction design process, axial compressors with reduced number of stages, shortened axial lengths, and rotor blisks have been implemented. However, shortening the compressor axial length and reducing the compressor stages typically worsens the stall behaviour. This is a challenge for the design of future combat air system engines, which are intended to be stable, performing, care-free, and light-weight, among other requirements. To meet such demanding system specifications, new jet engine design features are sought that supplement the stability margin of future aircraft engines.

Studies on the stall inception mechanism of axial compressors have long been addressed by many researchers. The early investigations into the rotating stall inception mechanism were mainly conducted by experiment. Camp & Day [1] classified the stall inception mechanism of a low-speed axial compressor into two types: spike type stall inception and modal type stall inceptions. Mitigating the onset of stall is among the design requirements of axial compressors. Gallimore et al. [2, 3] investigated the effect of aerofoil sweep and dihedral for a multistage axial flow compressor blading. The effects of sweep and dihedral blade were examined by computational simulations and experiments at the Whittle Laboratory, University of Cambridge. These studies led to implementing a design feature in the Rolls-Royce TRENT 500 turbofan that enhanced the flow instability. Vo [4] explored the alternative approach of active flow control by using plasma actuators to extend the operating range of an axial compressor. By performing experiments with a low-speed axial compressor test rig and by conducting numerical simulations on the same axial compressor it was shown that the actuators delay the compressor stall inception.

Another technique aimed at improving in the stability of the compressor is casing treatments. This is a passive flow control approach, by which the engine weight increase can be smaller than with equivalent active flow control techniques. Casing treatments have been investigated since at least 1971 [5]. The casing treatments reported in previous studies can be broadly classified into two types, that is, non-axisymmetric slots and axisymmetric grooves. Advanced non-axisymmetric slot designs were investigated by Schnell et al. [6]. Circumferential grooves provide lower gains in stall margin [5], but they do not show the compressor efficiency penalty of the non-axisymmetric slots. Currently, simple square grooves have been applied to the fan casing of the GE F110 turbofan engine [7]. Sakuma et al. [8] investigated numerically the influence of the position and depth of a single square groove on the performance of a transonic rotor developed by the National Aeronautics and

Space Administration (NASA). They found that a groove located at 0.2 axial chords downstream from the blade leading edge was the best position for this design feature. Cevik et al. [9] studied circumferential grooves with a sawtooth shape. Their work focused on decreasing the sensitivity of the compressor stability to the tip clearance height.

A further type of casing treatment is one that uses a recirculating channel. Koff et al. [10] use a channel in the casing fitted with aerofoils that aim to reduce the tangential velocity component of the flow through it. Hathaway [11] modelled the flow through an axial compressor with a recirculating type casing treatment by solving the one-dimensional mass balance equations between the channel inlet and the channel outlet. His application extends the operating range of the NASA axial rotor without producing an adiabatic efficiency drop. More recently, Dinh et al. [12] conducted a parametric study on the design of a recirculating type casing treatment. They varied the injection positions, the bleed position, and the width of the channel, to evaluate the influence on the compressor performance and managed to identify a useful range of parameters for which the rotor is able to operate at lower mass flow rate conditions.

The application of a recirculating type casing treatment is expected to improve the stable operating range, but the application of these treatments to a production engine compressor has not been reported yet. In this paper, the flow structure of a transonic axial compressor fitted with a recirculating type casing treatment is investigated by using Computational Fluid Dynamics. A targeted numerical analysis will provide useful insight on this new casing treatment for gas turbine engine designers. This will aid to establishing the design method of recirculating type casing treatments in production engines for high-speed jets.

## 2.0 NUMERICAL MODELLING

### 2.1 Benchmark test case

The rotor passage geometry of the NASA rotor 37 [13] is used in this study. A meridional plane sketch of the NASA rotor 37 is shown in Fig. 1. Table 1 summarizes the main design parameters of the NASA rotor 37.

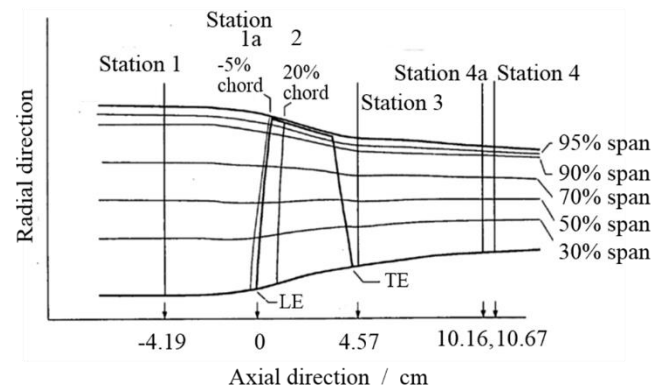


Figure 1. Meridional plane sketch of the NASA stage 37 rotor, from Dunham [13].

Table 1. Design parameters of the NASA stage 37 rotor, from Dunham [13].

		Design
Rotor total pressure ratio	-	2.106
Rotor polytropic efficiency	%	88.9
Number of rotor blades	-	36
Rotational speed $\omega_3$	rad s <sup>-1</sup>	-1800
Rotor inlet hub-to-tip diameter ratio	-	0.7
Blade aspect ratio	-	1.19
Tip relative inlet Mach number	-	1.4
Aerofoil profile		MCA
Tip clearance	mm	0.356

Station 1 and Station 4 in Fig. 1 are the axial planes used in experiments to measure the aerodynamic performance of the NASA rotor 37. NASA designed this axial compressor rotor as the first stage rotor of an eight-stage compressor having a total pressure ratio of 20, for an engine core. This rotor was experimentally tested at the NASA Glenn Research Center at Lewis Field, Cleveland, Ohio, to evaluate its performance characteristic. Details of the experimental measurements are provided by Dunham [13].

As the stage design total pressure ratio of 2.1 is relatively high compared to contemporary axial compressors, this compressor geometry is representative of highly loaded compressors, such as the ones used in high specific thrust engines of high speed aircraft. Although many contributions have used the NASA rotor 37 as test case, it is considered that several flow features are still not entirely explained.

## 2.2 Discretization of computational domain

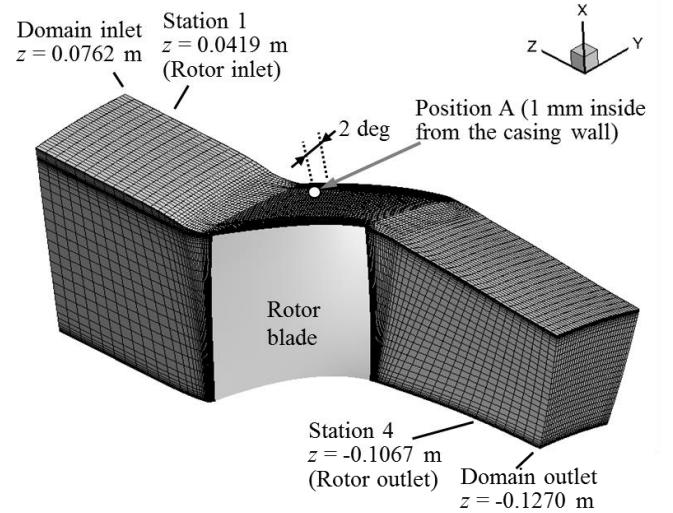
Figure 2 gives an overview of the computational domain and mesh through one passage of the NASA stage 37 rotor row. Fig. 2 (a) corresponds to 1/36<sup>th</sup> of the rotor full annulus. The computational domain inlet is located three times the axial length of the blade chord  $c_z$  upstream from the blade leading edge tip. The computational domain outlet is located three  $c_z$  downstream of the blade trailing edge tip. ANSYS ICEM CFD is used for generating a structured computational mesh, which is shown in Fig. 2 (a). In Fig. 2 (a), the mesh is shown coarsened by a factor of two in each spatial direction, for graphical rendering purposes. A  $5 \times 10^{-6}$  m constant height for the first cell normal to the solid surface is used throughout the domain, which achieves an average near-wall resolution of  $y^+ \approx 1.5$ . It is of interest to study the effect of the casing treatment in a configuration of a stall inception. To this end, the multi-passage computational domain of Fig. 2 (b) is built by replicating the one blade-to-blade passage mesh shown in Fig. 2 (a) for 12 times in the circumferential direction.

## 2.3 Description of flow solver

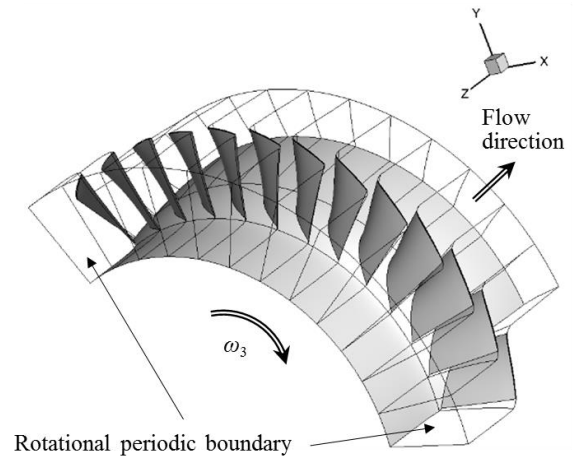
The calculations are run both as steady and as time-dependent Reynolds-Averaged Navier-Stokes (RANS) simulation with the realizable  $k$ - $\epsilon$  turbulence closure model [14]. To estimate the convective fluxes at the finite-volume unit cell boundaries throughout the computational domain, the flux difference split method by Roe is used, in combination with the approximate Riemann solver by Roe. To obtain higher accuracy in the spatial discretization, a

third-order spatial reconstruction scheme, the Monotone Upwind Scheme for Conservation Laws (MUSCL) provided by Van Leer et al. [15], is used. For steady-state simulations, time-marching iterations by Weiss [16] are conducted until a steady-state solution is reached. For time-dependent RANS simulations, a physical time discretization of second-order accuracy by Pandya et al. [17] and Turkel & Vasta [18] is applied. Pseudo-time advancement is performed by local time stepping that is Courant number limited to 5. For time-dependent RANS simulation, one blade pitch rotation is produced by integrating over 20 time steps. An under-relaxation factor of 0.8 is used for the specific turbulent kinetic energy  $k$  and for the specific dissipation rate of specific turbulent kinetic energy  $\epsilon$  to improve the numerical stability of the computation.

The working fluid is air assumed as a compressible ideal gas. The specific heat capacity at constant pressure  $c_p$  is set to  $1,004 \text{ J kg}^{-1} \text{ K}^{-1}$ . The ratio of specific heat capacities  $\gamma$  is set to 1.4 based on the literature [19]. Sutherland's law is applied to estimate the molecular viscosity of air. The air thermal conductivity is calculated according to Tsederberg [20].



(a) Structured mesh for the one blade-to-blade passage simulation.



(b) Computational domain of 12 blade-to-blade passages.

Figure 2. Schematic of the computational domain and mesh.

## 2.4 Boundary conditions

Table 2 shows the flow conditions used in this study. The total pressure  $P_{0in}$ , the total temperature  $T_{0in}$ , and the turbulence intensity  $I$  at the computational domain inlet are specified based on the experimental test inflow conditions reported by Dunham [13]. The turbulence length scale  $l$  is estimated by the relevant dimension of the diameter of the inlet duct.

At the computational domain inlet, an axially uniform inflow is imposed based on the inflow stagnation pressure and on the inflow stagnation temperature. The inflow is turbulent and uniform inflow  $k$  and  $\varepsilon$  fields are prescribed based on the turbulence intensity  $I$  and on the turbulent length scale  $l$ , as previously defined.

The static pressure at the computational domain outlet of Fig. 2 is specified as the outflow boundary condition. For steady RANS simulations, the static pressure is imposed under the condition of radial equilibrium. For time-dependent RANS simulations, a macroscopic pressure resistance model [21] is applied to the outlet boundary in order to model the pressure drop during the stall inception process, which is defined by:

$$P_{out} = P_{0in} + \frac{1}{2} c_t \bar{\rho} \bar{u}_a^2 \quad (1)$$

where  $c_t$  is the pressure resistance coefficient of the downstream throttle valve which is used in experiment to set the operating condition of the compressor rotor,  $\bar{\rho}$  is the mass-averaged fluid density at the computational domain outlet, and  $\bar{u}_a$  is the mass-averaged axial velocity at the computational domain outlet. All other variables are extrapolated from the computational domain interior. On the surfaces of the aerofoil, the shroud, and the hub, no-slip adiabatic wall boundary conditions are applied. A near-wall modelling method that combines a two-layer model with wall functions is used for the estimation of the flow state at the first interior cell. Rotational periodic boundary conditions are applied at the pitchwise periodic flow boundaries. In the analysis of the stall inception process, 12 blade-to-blade passages are modelled to capture the propagation of the rotating stall among the rotor passages.

After obtaining numerically converged results at a back pressure of  $P_{out} = 101.325$  kPa, using this result as the initial condition, the static pressure at the domain outlet is gradually increased up to the stall inception. The last increment before the stall inception is 0.3% or less of the atmospheric pressure. Convergence is deemed to be achieved when the change during 2,000 iterations in the mass flow rate is 0.001% of the inflow. This is achieved by performing between 10,000 and 59,000 iterations in the benchmark case, depending on the specific rotor back pressure value that is imposed.

Table 2. Flow conditions used for the numerical modelling.

Inlet		
Total pressure $P_{0in}$	kPa	101.325
Total temperature $T_{0in}$	K	288.15
Turbulence intensity $I$	%	3
Turbulence length scale $l$	m	0.0114
Outlet		
Static pressure $P_{out}$	kPa	Varied from 101.3 to stall inception.

## 2.5 Discretization sensitivity analysis

To estimate the error caused by the spatial discretization on the flow predictions, a mesh convergence study is carried out using Richardson's extrapolation that is generalized by Roache [22]. In this work, three meshes are used to discretize the rotor passage with a constant refinement ratio  $r_m = 2.0$ . These are a coarse mesh of  $0.7 \times 10^6$  nodes (mesh A), a mesh of intermediate spatial refinement of  $1.5 \times 10^6$  nodes (mesh B), and a fine mesh of  $3.1 \times 10^6$  nodes (mesh C). In the present work, two grid convergence indices (GCI) are calculated. The first GCI is calculated based on the adiabatic efficiency of the rotor blade row and the second GCI is based on the local value of the static pressure near the rotor pressure side tip at the near-stall operating condition. The location of the local static pressure monitor is denoted as Position A in Fig. 2(a). It is where the computational fluid dynamic simulation predicts the breakdown of the tip leakage vortex, which is identified as the main driver of the stall inception in this rotor. The rotor blade row adiabatic efficiency computed with each of the three meshes is 85.675%, 85.895%, and 85.997%. The GCI computed from the adiabatic efficiency predicted with the coarse mesh (mesh A) and that with the intermediate mesh (mesh B) is 0.273%. This is higher than the GCI computed from the adiabatic efficiency predicted with the intermediate mesh (mesh B) and that with the fine mesh (mesh C), which is 0.126%. The difference between the adiabatic efficiency  $\eta_n$  predicted using the  $n^{\text{th}}$  mesh and the one obtained from Richardson's extrapolation  $\eta_R$  is used to define the relative error as  $e = \eta_n \eta_R^{-1} - 1$ . Based on this, the magnitude of adiabatic efficiency error for the mesh B is estimated to be 0.218%. The GCI computed from the local static pressure at Position A in Fig. 2 (a) predicted with mesh A and that with mesh B is 0.117%, which is higher than the GCI computed from the local static pressure at the position A predicted with the intermediate mesh (mesh B) and that with the fine mesh (mesh C), which is 0.011%. The estimated magnitude of the local static pressure error for mesh B is 0.094%, which is sufficiently small for the purpose of this study. Specifically, this study uses computational fluid dynamics to estimate the performance changes from variances of the compressor passage geometry as opposed to absolute performance values. This allows accepting the stated GCI errors. From this result, the intermediate mesh (mesh B) is selected for this study.

### 3.0 MODEL VALIDATION AND STALL INCEPTION IN THE HIGHLY LOADED AXIAL COMPRESSOR

#### 3.1 Model validation

Figure 3 compares the radial profiles of circumferentially mass-averaged total pressure at Station 1 and at Station 4, of tangential velocity at Station 4, and of flow angle at Station 4, between CFD and experiment. The radial profiles calculated by the steady RANS with the realizable  $k-\varepsilon$  turbulence closure model are shown in Fig. 3 by black solid lines. The radial profiles predicted by the time-dependent RANS are also shown by grey dashed lines in the same figure. For time-dependent RANS, the radial profiles are calculated by the average of four equispaced time points during one pitch blade rotation, at increments  $\Delta t = 2\pi / (36 \times 5 \times \omega_3)$

There is no significant difference among the predictions by all three models at the rotor blade inlet (Station 1), where the three velocity profiles overlap each other. These profiles are in good agreement with the experimental results, shown by the symbols. At the outlet of the rotor blade (Station 4), the flow analysis with the realizable  $k-\varepsilon$  turbulence closure model shows good agreement with experiment, both with the steady simulation and with the time-dependent simulation. To show the sensitivity of the predictions to the choice of the turbulence closure model, the radial profiles calculated by the steady RANS with the  $k-\omega$  SST turbulence closure model are drawn in the same figure by black dash-dotted lines. As shown in Fig. 3(c) and (d), the simulation with the  $k-\omega$  SST turbulence closure model predicts a too intense tip leakage flow, which gives a tangential velocity and flow angle different from the experimental measurements over the span fraction range  $0.9 \leq h_r/H_r \leq 1.0$ . As the NASA rotor 37 used in this study is predicted to stall due to a collapse of the flow structure on the rotor tip side [24], the simulations presented hereafter are conducted with the realizable  $k-\varepsilon$  turbulence closure model, which seems to provide a more appropriate prediction of flow structure on the rotor tip side. The results with the  $k-\omega$  SST model are somewhat unexpected, given that this model does not require artificial numerical damping for  $\omega$  on approach to the wall boundaries, unlike with  $\varepsilon$  in the realizable  $k-\varepsilon$  model. Whereas the reduced reliance on a calibrated wall damping function would intuitively give a modelling advantage, in this specific application, it appears that predictions closer to experiment are obtained by the realizable  $k-\varepsilon$  model.

Table 3 compares the choked mass flow rate and the normalized mass flow rate at near-stall condition between CFD and experiment. Corresponding numerical predictions from the literature are also shown in Table 3.

The choked mass flow rate is somewhat smaller than in NASA's experiment. This agrees with the other predictions from the literature shown in Table 3. The mass flow rate at the near-stall condition predicted in this work is likewise slightly smaller than in the experiment. The stable operating range predictions from the current numerical model are shown in Table 3 to lie within the spread of the predictions from the literature.

The results of Fig. 3 and Table 3 indicate that the current steady RANS simulation with the realizable  $k-\varepsilon$  turbulence model is capable of evaluating the performance of the NASA rotor 37 for the purpose of assessing different casing treatments.

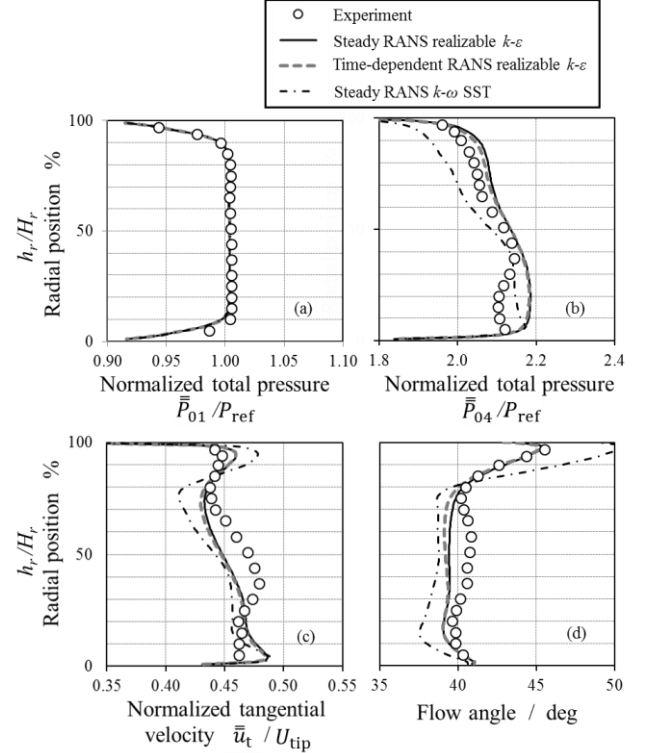


Figure 3. Circumferentially mass-averaged radial profiles at Station 1 and at Station 4 showing a comparison between CFD and experimental data reported by Dunham [13], and Arima et al. [23].

Table 3. Comparison in choked mass flow rate and the mass flow rate at the near-stall condition.

	Choked mass flow rate / $\text{kg s}^{-1}$	Normalized mass flow rate at near-stall condition %
Experiment	20.93	91.9
(Stalled flow)		
Steady RANS		
Kawase & Rona	20.82	91.4
Arima et al. [23]	20.77	92.4
Sakuma et al. [8]	20.78	92.1
Hah [25]	20.92	92.3
Kim et al. [26]	-	90.9
Time-dependent RANS		
Kawase & Rona	20.84	91.2
Zhu et al. [27]	-	87.8

#### 3.2 Time dependent analysis of rotor tip stall

To establish an effective design approach for improving the compressor stability, it is of interests to observe the flow

features that characterize rotor tip stall. Figure 4 shows by colour iso-levels the time change of fluid density at 0.99 blade span at different times through the time-dependent RANS simulation. The time change of fluid density shown in Fig. 4 is calculated as:

$$\frac{d\rho}{dt} = \frac{\rho_{kt} - \rho_{kt-1}}{4.85 \times 10^{-6}} \quad (2)$$

where  $t$  denotes the physical time and  $kt$  denotes the physical time level. In the time-dependent RANS simulation shown in Fig. 4, the mass flow rate at the domain inlet and at the domain outlet shows a sharp decrease from  $18 \text{ kg s}^{-1}$  to  $12 \text{ kg s}^{-1}$  after  $t_{\text{rev}} = 8.0$  revs. Thus, Fig. 4 shows the flow transition around the rotor blade row before the sharp decrease in the mass flow rate due to the stall inception. The regions where the fluid density increase are coloured in red, and the regions where the fluid density decrease are coloured in blue. The iso-level boundary is drawn with solid lines every  $10 \text{ kg m}^{-3}$   $\text{s}^{-1}$ .

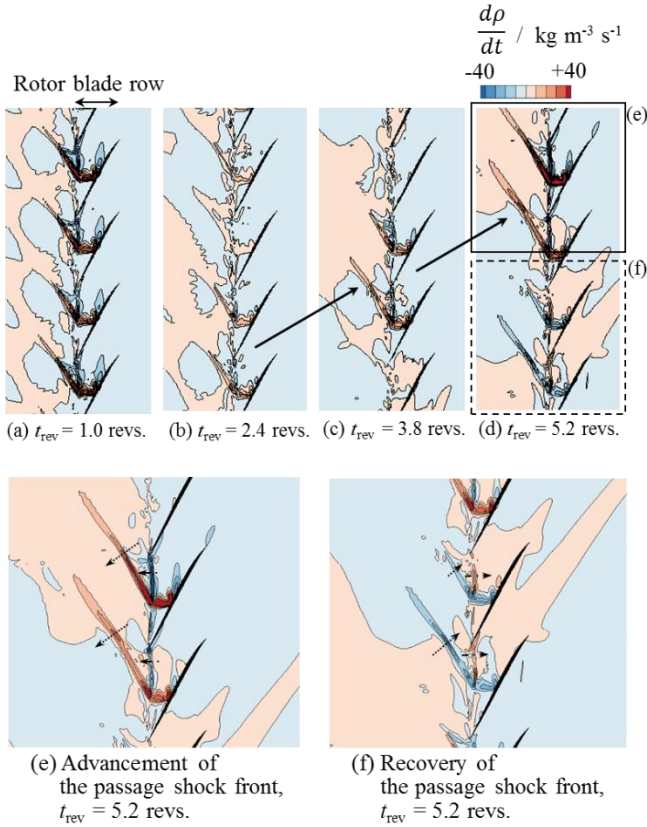


Figure 4. Distribution of the time change of fluid density at 0.99 blade span, showing the rotating stall inception propagation in the opposite direction of blade rotation.

At  $t_{\text{rev}} = 1.0$  revs., as shown in Fig. 4(a), all the leading edge shockwaves shift upstream, due to the increase of the back pressure. As the passage shockwave moves upstream, the fluid density downstream of the shockwave increases, which is shown as red regions in the Fig. 4(a). At  $t_{\text{rev}} = 2.4$  revs., weaker time changes in fluid density are predicted at some passage shockwaves. This feature propagates in the opposite direction to the blade rotation direction. As shown in Fig. 4(b), (c), and (d), the amplitude of the density time change

grows gradually as the physical time increases and eventually causes a large-scale flow-structure breakdown through the rotor. Figure 4(e) and (f) are enlarged views of Fig. 4(d). Figure 4(e) is of a region enclosed by a solid line in Fig. 4(d), and Fig. 4(f) is of a region enclosed by a dotted line in Fig. 4(d). Figure 4(e) shows the leading edge shockwaves moving forward, as indicated by dotted arrows. Following this, by propagating the flow disturbance, these shockwaves move back, as indicated by dotted arrows in Fig. 4(f). There are also significant time changes in fluid density where the interface, or confluence, forms between the inflow and the reversed tip leakage flow from the rotor tip clearance. In conjunction with the advancement of the shockwaves shown in Fig. 4(e), the interface moves upstream, which causes a negative time change in the fluid density downstream of the interface. By contrast, Fig. 4(f) shows the passage shockwave and the interface moving downstream at the same physical time level as Fig. 4(e).

Figure 5 shows streamlines of the relative velocity and flow blockages at different times. Figure 5(c) documents the flow behaviour after the sharp drop in the mass flow rate. It shows a significant change in the flow structure from the un-stalled state. The streamlines in Fig. 5 are traced from seeds placed inside the tip clearance and at the rotor inlet. The green streamlines are drawn from the seeds placed at 0.85 tip clearance height of each blade. The seeds for the orange streamlines are arranged in the circumferential direction every one degree from the rotor blade LE, at the height of the blade tip in the radial direction. The boundary surfaces of the flow blockage are identified by iso-surfaces of zero axial velocity. These boundaries are drawn by a translucent blue surface.

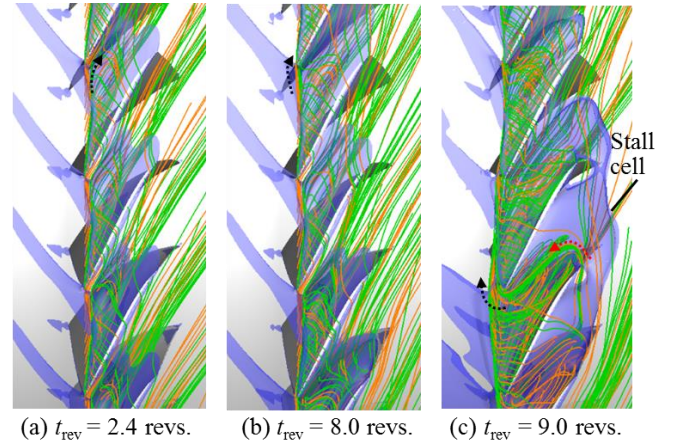


Figure 5. Streamlines near the casing with flow blockage, showing the flow spillage and backflow inside the small stall cell.

At  $t_{\text{rev}} = 2.4$  revs., before the flow is stalled, the orange streamlines flow into the blade passage passing through the gap between the pressure side of the rotor blade and the interface, as indicated by dotted arrow in Fig. 5(a). At  $t_{\text{rev}} = 8.0$  revs. at which the disturbance in the air density shown in Fig. 4(d) grew and propagated, some orange streamlines are pushed forward by the interface and flow into the adjacent rotor flow path, as highlighted by dotted arrow in Fig. 5(b). Figure 5(c) shows an even larger scale breakdown of the flow

in the passage at  $t_{rev} = 9.0$  revs. At this time, the flow structures in successive blade-to-blade passages are very different from one another. The green streamlines from the tip clearance also pour into the adjacent flow path passing upstream of the adjacent blade leading edge. Furthermore, as shown by red arrow in Fig. 5(c), intense backflow occurs from the trailing edge of the rotor blade. At  $t_{rev} = 9.0$  revs., a large blockage spreads among two or three rotor passages associated with this backflow, which seems to be a small stall cell. The occurrence of the backflow from the rotor trailing edge and the spillage from the tip clearance is consistent with the flow feature during the stall inception suggested by Vo et al. [28].

## 4.0 RECIRCULATION CHANNEL CASING TREATMENT

### 4.1 Recirculation channel concept

Rotor blades and axial flow compressors can feature a rotor tip type stall, by which reverse flow at the rotor tip progressively extends over the blade span. As discussed in Section 3.2, the rotor tip leakage promotes the onset of this reverse flow. By controlling the reversed flow near the casing, a delay in the tip stall onset is sought. Figure 6 describes the concept of a self-adjusting passive control technique for the rotor tip leakage. In Figure 6, one flow passage of the NASA rotor 37 is rendered in three dimension. An axisymmetric channel is designed on the casing wall over the rotor blade. This channel design broadly draws from a detail of the one-way valve by Nikola Tesla [29].

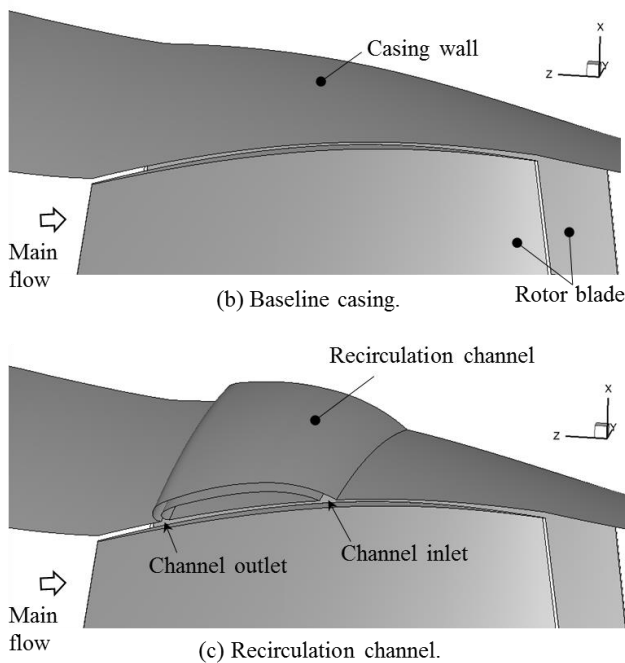


Figure 6. Overview of the casing treatment applied over the NASA stage 37 rotor.

A recirculating flow is induced in this recirculation channel (RC) by the pressure difference between the suction side and the pressure side of a rotor blade. This pressure difference is

enhanced by the axial pressure gradient through the rotor passage. The induced flow is intended to seal the tip leakage flow near the casing wall. The channel outlet is of a subsonic nozzle shape to obtain a high momentum with a small recirculation mass flow rate. This leakage flow mitigation approach does not require reducing the rotor tip clearance. Therefore, this design is less likely to suffer from blade tip rubbing issues than more established flow resistive type approaches, such as labyrinth seals, which rely on small tip clearances.

### 4.2 Numerical modelling of the recirculation channel

The flow through one passage of the NASA rotor 37 with circumferential recirculation channel is modelled by the computational mesh shown in Fig. 7. The structured mesh for the recirculation channel is first created as a stand-alone mesh and then it is abutted to the main passage mesh by defining the interface between the two meshes.

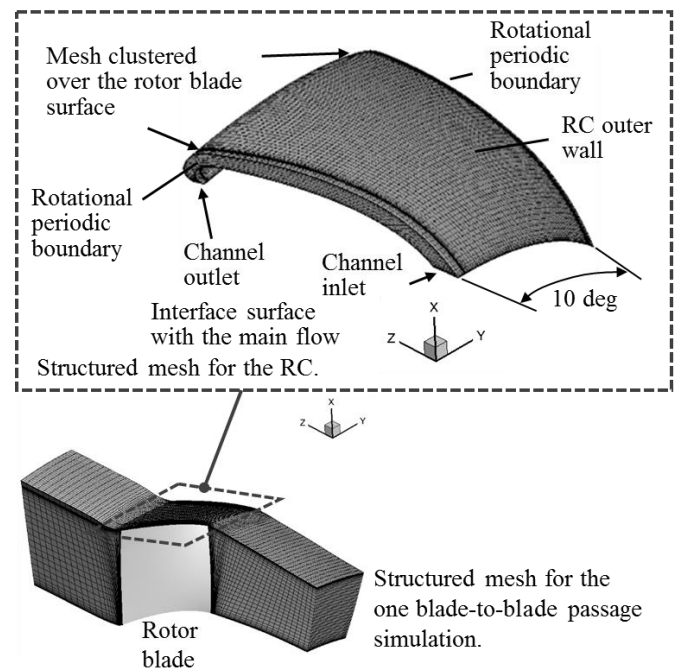


Figure 7. Schematic of structured mesh for the recirculation channel applied over the NASA stage 37 rotor.

The structured mesh of the recirculation channel shown in Fig. 7 is generated by ANSYS ICEM CFD. As in the computational mesh of the main flow passage, 10 degrees in the circumferential direction, which is one blade pitch of the rotor blade row, are modelled. A  $5 \times 10^{-6}$  m constant height for the first cell normal to the solid wall is used. In order to reduce the difference in size, the cells in the recirculation channel arranged in the vicinity of the blade surface are clustered. The number of nodes used for discretizing the recirculation channel domain shown in Fig. 7 is  $0.5 \times 10^6$ .

### 4.3 Recirculation channel variants

The flow inside the Recirculation Channel (RC) is activated by the pressure difference between the channel inlet and the channel outlet. As this pressure difference is enhanced by the

axial pressure gradient through the rotor passage, the axial length of the RC is likely to be an important factor in determining the RC performance. Therefore, a parametric study on the RC length is carried out to evaluate its effect on the compressor performance. Increasing the channel length is expected to enhance the compressor rotor stability. In this study, recirculation channels with six different axial lengths are tested, as shown by the meridional plane schematic of Fig. 8. Table 4 lists the axial location and the axial length of each RC. The definitions of the axial location and of the axial length of the RC are shown in Fig. 8. In Fig. 8, each RC case is denoted by an arrow with its name at each channel inlet. Case #0 RC is applied at approximately 20% axial chords downstream from the blade leading edge in the axial direction, since in Sakuma [8] this single rectangular groove for the NASA rotor 37 gave the best stall margin among the investigated axial locations. The position of the channel outlet is the same in all cases. The channel geometry of each case is generated by locating the channel inlet downstream in 0.1 axial chord increments. The stall inception is determined numerically for all cases by progressively increasing the exit pressure boundary condition.

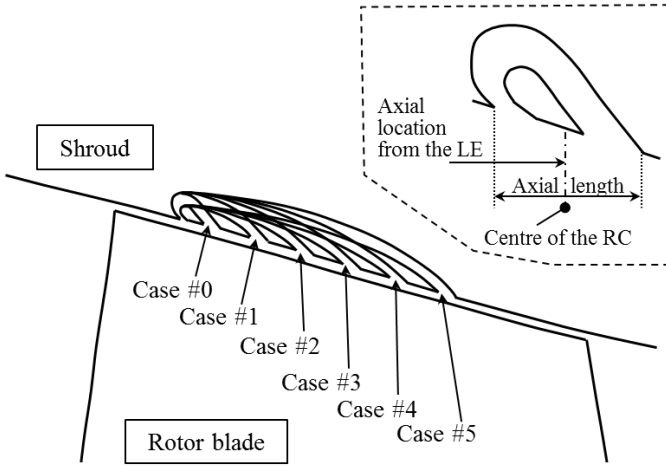


Figure 8. Schematic of locating the RC with different axial lengths on the meridional plane.

Table 4. Parametric study of the length of the recirculation channel on the rotor shroud wall.

Case	Axial location % of $c_z$	Axial length % of $c_z$
Case #0	18.2	8.5
Case #1	23.1	18.4
Case #2	28.1	28.3
Case #3	33.1	38.3
Case #4	38.1	48.3
Case #5	43.1	58.4

## 5.0 EFFECT OF THE RECIRCULATION CHANNEL ON A HIGHLY LOADED AXIAL COMPRESSOR ROTOR

### 5.1 Overall compressor performance characteristics

The flow in the computational domain of Fig. 7 is predicted by steady RANS simulations using the same procedure and main passage boundary conditions as the one used in Section 3.1 for the validation of the baseline numerical model. Figure 9 shows the comparison of the compressor performance characteristics among the six test cases. Figure 9(a) uses the same legend and abscissa as Fig. 9(b). The total pressure ratio in Fig. 9(a) is calculated by the ratio of the total pressure predicted at Station 4 of Fig. 2(a) to the reference upstream total pressure given by Dunham [13]. The adiabatic efficiency is calculated by:

$$\eta = \left[ \frac{(\bar{P}_{04}/\bar{P}_{01})^{(\gamma-1)/\gamma} - 1}{(\bar{T}_{04}/\bar{T}_{01}) - 1} \right] \times 100 \quad (3)$$

The choked mass flow rate  $\dot{m}_{choked}$  predicted in the CFD of the Baseline (BL) case is used to normalize the abscissa. The predicted limit of the stable operating range for each case is marked by the grey filled symbol. The stable operating range of the compressor rotor is indicated by an arrow for each test case at the bottom of Fig. 9(a).

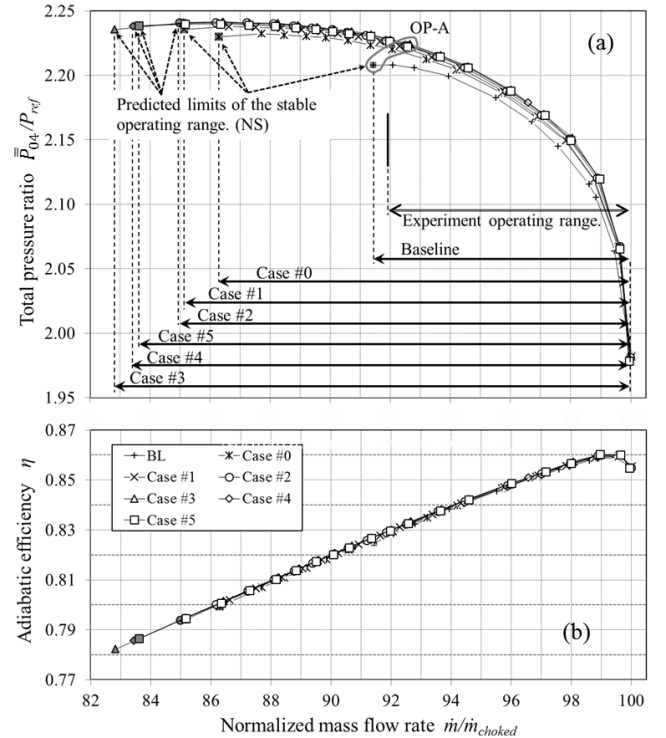


Figure 9. Overall compressor performance characteristics showing the influence of the RC length.

As shown in Fig. 9(a), the operating range of the compressor rotor in terms of the mass flow rate increases from Case #0 to Case #3. However, when the channel length is increased

beyond Case #3, the operating range gradually decreases as shown in Case #4 and in Case #5. As shown in Figure 9(a), the operating points at the OP-A condition in Case #4 and in Case #5 sit at a higher mass flow rate than Case #0. In Case #3, Case #4, and Case #5, the compressor rotor reaches the left limit of the stable operating range at the same back pressure setting of  $P_{out} = 129.8$  kPa. These shows that the positive effect of RC extending the rotor operating range is probably saturated when the RC length is  $\geq 38.3\%$  of  $c_z$ . Among these test cases, Case #3 is predicted to have the best stall margin. Figure 9(b) shows that the rotor adiabatic efficiency is substantially unaffected by the presence of the RC.

## 5.2 Analysis of the passage flow structures

Figure 10 visualizes the flow structures through the recirculation channel casing treatments by streamlines of the absolute velocity. For all the cases shown in Fig. 10, the streamlines are traced by the simulations at the operating condition OP-A shown in Fig. 9(a). These streamlines are drawn from the seeds which are placed at the channel inlet and at the channel outlet.

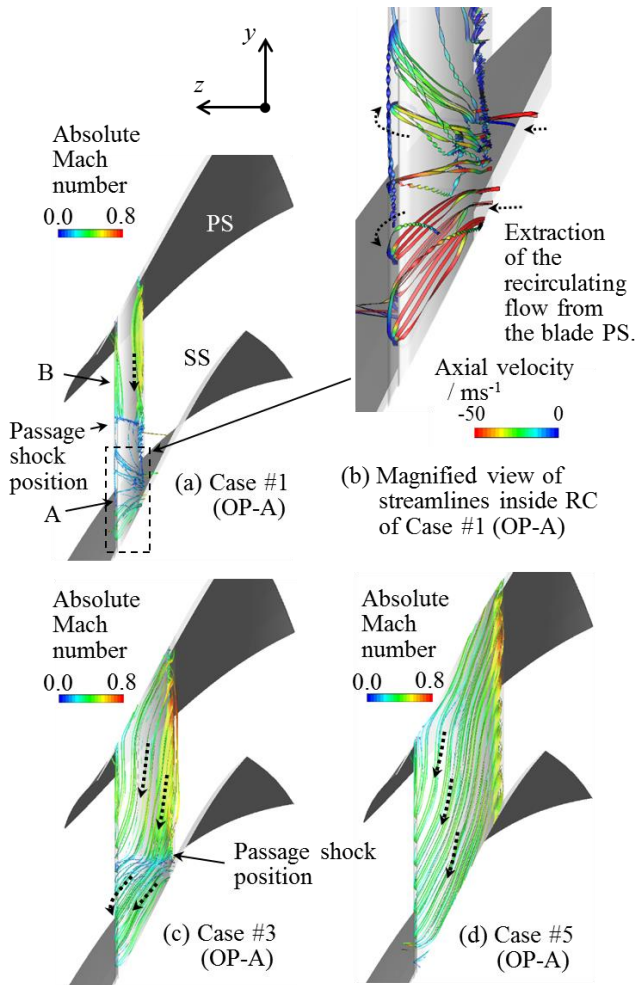


Figure 10. Streamlines showing the flow structure inside the RC with three different channel lengths. Passage viewed from the top towards the hub in the radial direction. Casing surface and outer wall of the RC made transparent for illustration purposes.

In Case #1, the flow recirculation occurs inside the casing channel only in the vicinity of the suction side of the rotor blade as labelled by “A” in Fig. 10(a). On the pressure side of the rotor blade across the passage shockwave, where labelled by “B” in Fig. 10(a), significant recirculating flow does not occur inside RC, since the circumferential velocity component toward the suction side of the rotor blade is dominant, as indicated by dotted arrow.

Figure 10(b) shows an enlarged view of the dashed-line inset of Fig. 10(a), which is where the rotor blade is passing radially below the RC. The recirculating channel streamlines in Fig. 10(b) are coloured by the axial velocity. Figure 10(b) shows that tip clearance flow from the blade pressure side (PS) is sucked at the recirculation channel inlet and it is injected into the main flow passage at the recirculation channel outlet. As indicated by the arrow call out in Fig. 10(c), in Case #3, the passage shockwave is located upstream of the casing channel inlet over most of the passage pitch, at the OP-A operating condition of Fig. 9(a). This increases the pressure difference between the channel inlet and the channel outlet. In Fig. 10(c) and (d), recirculating flow occurs over most of the passage pitch, inside the RC, as indicated by dotted arrows. The absolute Mach number of the recirculating flow is higher in Case #5 than in Case #1, which increases the recirculating flow momentum injected into the main flow passage at the channel outlet.

Figure 11 shows how the flow blockage created in the main passage changes with the axial location of the RC. The boundary surfaces of the flow blockage are identified by iso-surfaces of zero axial velocity. These boundary surfaces are coloured by the radial distance from the casing wall of the baseline geometry normalized by the radial height of the main flow passage. Contour lines are drawn on these surfaces by black lines every 0.25% of the passage radial height. The rotor tip clearance is about 0.8% of the passage radial height. The blockage created by the rotor tip leakage is visualized at two different operating points: OP-A and NS of Fig. 9.

Figure 11(a) visualizes the flow blockage in the BL case at its near-stall condition (OP-A). This blockage is caused by the volume between the zero-velocity iso-surface of Fig. 11(a) and the casing being filled by low-velocity fluid from the breakdown of the tip leakage vortex. This is an unwanted feature. At the OP-A condition, the spread of the flow blockage in the main passage is mitigated by applying the recirculation channel casing treatment. Furthermore, the size of the flow blockage is significantly reduced by applying a longer casing channel, as shown in Fig. 11(c) and in Fig. 11(d). The call-out arrows in Fig. 11(c) and (d) indicate that the reversed flow on the casing surface downstream of the channel outlet is visibly reduced. The recirculation channel in this study is designed for suppressing the reversed flow on the casing wall by opposing the reversed flow at the channel outlet. At OP-A condition, in Case #3 and #5, the penetration of the RC nozzle outflow towards the hub is insufficient. This allows a small blockage to remain in the main passage, as indicated in Fig. 11(c) and (d).

## 6.0 TIME-DEPENDENT ANALYSIS OF ROTOR TIP STALL INCEPTION

### 6.1 Overall compressor performance characteristics

Since the stall inception of axial compressors is an inherently unsteady process [30], it is of interest to confirm the effectiveness of the recirculating casing treatment by performing time-dependent RANS simulations using the time-resolved numerical approach and boundary condition described in Section 2.0. Due to their computational cost, time-dependent RANS simulations were performed only for the baseline (BL) case and the recirculation channel (RC) case of Case #3 in Fig. 8. Figure 12 compares the overall compressor performance characteristics predicted by steady RANS and by time-dependent RANS simulations. Figure 12(a) uses the same abscissa as Fig. 12(b). Both in the BL case and in the RC case, the total pressure ratio and the adiabatic efficiency obtained by the time-dependent RANS simulations closely follow the trends obtained by the steady RANS simulations. For both the BL case and the RC case, the left limit of the stable operating range is predicted by 12 blade-to-blade passages time-dependent RANS simulations. For both the BL case and the RC case, the near-stall condition is obtained in the time-dependent RANS simulations at a slightly lower normalized mass flow rate than in the steady RANS simulations. This agrees with the finding by Vo [28] who obtained a wider operating range by time-dependent RANS simulations than by the steady RANS simulations. The stall margin improvement from the BL case to the RC case predicted by time-dependent RANS simulations is 8.89%, which is close to 9.11% predicted by the steady RANS simulations. The stall margin is calculated by Equation 4 used in [8] and in [30].

$$SM = \left[ 1 - \frac{\dot{m}_{NS} \times (\bar{P}_{04}/\bar{P}_{01})_{PE}}{\dot{m}_{PE} \times (\bar{P}_{04}/\bar{P}_{01})_{NS}} \right] \times 100 \quad (4)$$

where  $\dot{m}_{NS}$  denotes the mass flow rate at the near-stall condition, and  $\dot{m}_{PE}$  denotes the mass flow rate at the peak efficiency condition.

This provides confidence that the performance improvements provided by the RC casing treatment as predicted by steady RANS simulations are retained in the time-resolved flow model.

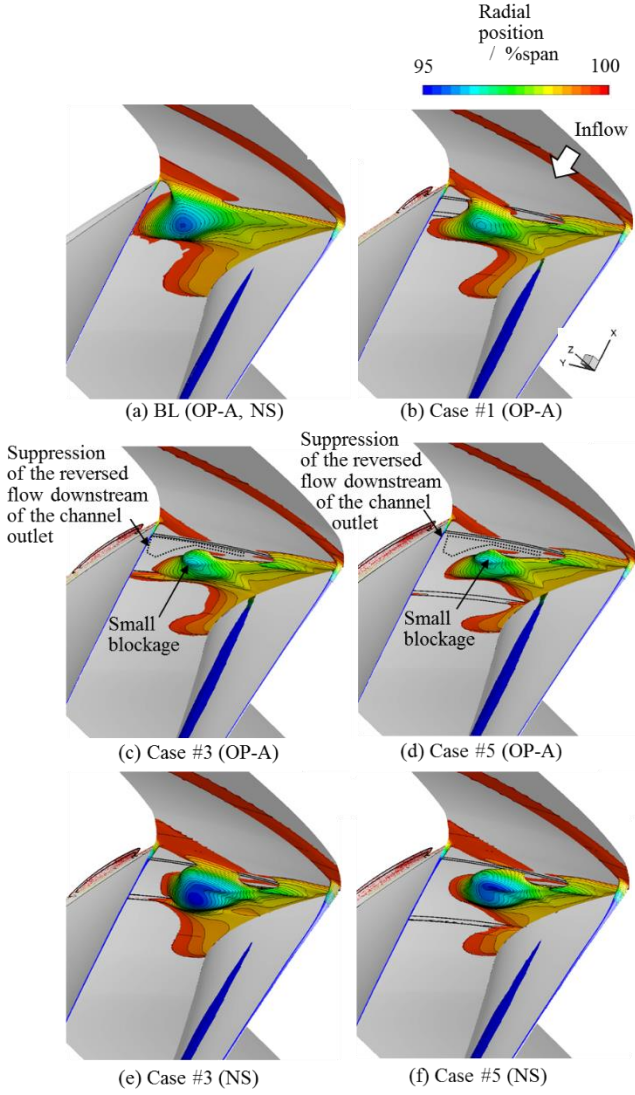


Figure 11. Visualization of the flow blockage mitigation on the shroud surface by the RC with different RC axial lengths. Passage viewed from the hub towards the casing, approximately in the radial direction.

The flow blockage predicted in Case #3 and in Case #5 at the near-stall (NS) condition is shown in Fig. 11(e) and (f). Figure 11(e) and (f) show that significant flow blockage occurs mid-way pitchwise between two blades near the casing wall. The blockage spreads radially further inwards than the blockage predicted in the baseline (BL) case at the near-stall condition shown in Fig. 11(a). On the other hand, the blockages in Case #3 and Case #5 still seem to be far away from the pressure side of the adjacent rotor blade. Therefore, in these results obtained by steady RANS simulations, it is still difficult to identify how the compressor rotor reaches the stall inception in Case #3 and in Case #5. To clarify the difference in the flow behaviour during the stall inception between the BL case and the RC case, a further investigation is conducted by multi-passage time-dependent RANS simulations.

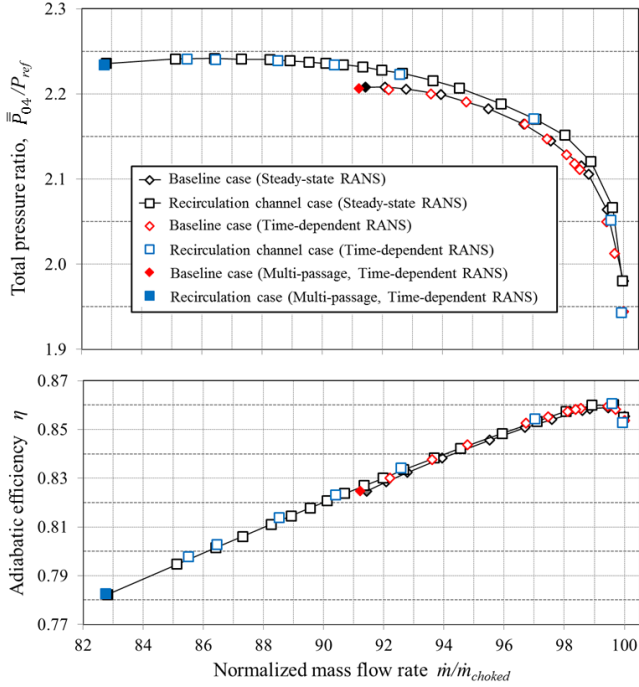


Figure 12. Comparison of overall compressor performance characteristics between steady RANS and time-dependent RANS.

## 6.2 Flow development during the stall inception

The process leading to the compressor stall is illustrated by the predicted time-resolved axial flow velocity distributions at 0.99 blade span in Fig. 13. Figure 13(a) to (d) show the simulation results of the baseline (BL) case. Figure 13(e) to (h) show corresponding results of the recirculation channel (RC) case that is shown in Fig. 12. The axial positions of the channel inlet and of the channel outlet are shown respectively by grey and black dotted arrows on the top of Fig. 13(e) to (h). In order to clarify the regions of backflow where the axial flow velocity is less than  $0 \text{ m s}^{-1}$ , the  $u_a = 0 \text{ m s}^{-1}$  contour is set to border blue and yellow areas. In the yellow areas,  $u_a < 0 \text{ m s}^{-1}$ . This makes the  $u_a = 0 \text{ m s}^{-1}$  contour stand out. Over the casing wall, a substantial area is wetted by reversed flow. As shown in Fig. 13(a), the reverse flow regions extend from the blade leading edge until about the rotor mid-chord. Upon breaking down, the tip leakage vortex generates this reversed-flow region. This low velocity region effectively creates a passage blockage between the rotor blades. As indicated in Fig. 13(b), the reversed flow region due to the vortex breakdown grows over time in the direction of the red dotted arrow between the aerofoils in the main passage. In Fig. 13(c), the area of the reversed flow between the aerofoils becomes larger and a distinctive backflow occurs in front of the leading edge of some rotor blades, as indicated by red dotted circles in Fig. 13(c). At  $t_{\text{rev}} = 8.0 \text{ revs.}$  shown in Fig. 13(d), the size of the reversed flow region significantly differs between the rotor passages. The reversed flow region between the rotor blades grows and decays cyclically pitchwise, through successive passages. This pitchwise cycle propagates in the direction opposite to the rotor rotation.

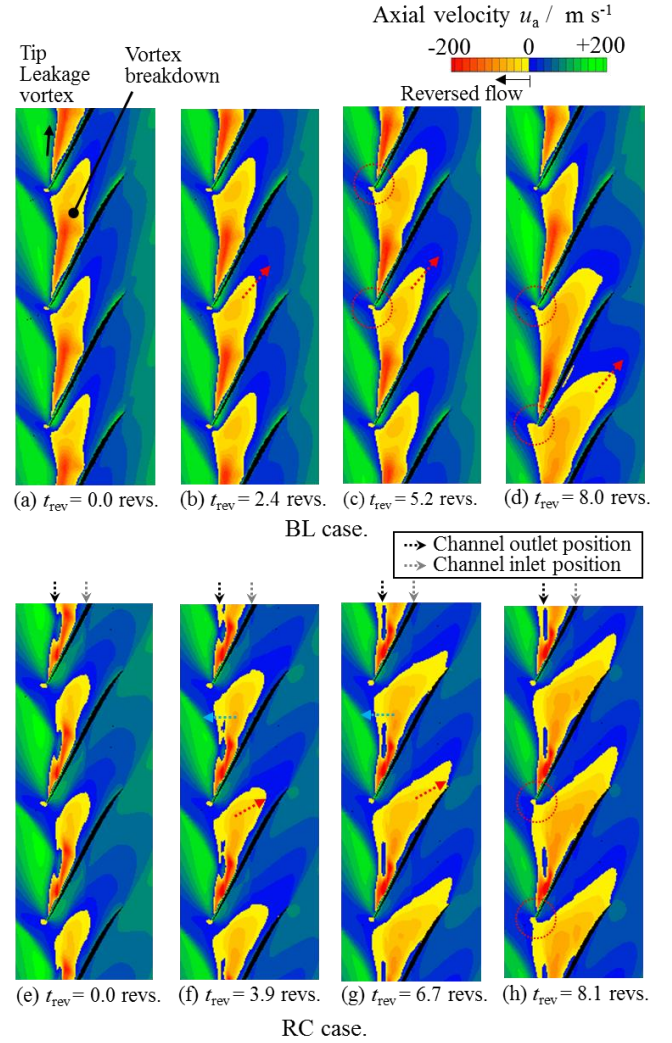


Figure 13. Axial velocity distribution at 0.99 blade span, showing reversed flow around the blade leading edge.

In the RC case, as shown in Fig. 13(e), the reversed flow is mitigated by the RC, which produces a smaller reversed flow area than in Fig. 13(a). In the RC case, the reversed flow area develops downstream over time, as indicated by red dotted arrows in Fig. 13(f) and (g), but the reversed flow area in the RC case spreads closer the suction side of the rotor blade compared to the BL case. This difference in the development of the reversed flow is probably given by the recirculating flow injection from the RC pushing the reversed flow axially downstream, through the passage. By this, as shown in Fig. 13(g), the distance between the reversed flow region and the pressure side of the adjacent rotor blade is kept wider than in the baseline case of Fig. 13(c). In Section 5.2, steady RANS simulations predict that the RC mitigates the development of the reversed flow over the casing and that the RC prevents the flow blockage from reaching the pressure side of the adjacent rotor blade. Figure 13(g) shows that this attractive effect of the RC is still obtained at  $t_{\text{rev}} = 6.7 \text{ revs.}$  However, from  $t_{\text{rev}} = 0.0 \text{ revs.}$  to  $t_{\text{rev}} = 6.7 \text{ revs.}$ , the reversed flow area is growing upstream of the RC outlet as highlighted by blue dotted arrows in Fig. 13(f) and (g). At  $t_{\text{rev}} = 8.1 \text{ revs.}$  shown in Fig. 13(h), the reversed flow area on the upstream side of the RC outlet grows in the pitchwise direction and eventually

backflow occurs ahead of the leading edge of some rotor blades, as indicated by red dotted circles in Fig. 13(h).

In Section 5.1, as shown in Fig. 9, a further improvement in the compressor operating range is not obtained in Case #4 and Case #5, even though the casing channel is longer than Case #3. As stated in Section 5.2, in steady RANS simulations, the time-dependent mechanism leading to stall inception is not captured, although the steady RANS simulations still gave information on steady flow features that closely correlate to this mechanism, such as the extent of the reversed flow region at the casing. Following this, time-resolved RANS simulations revealed that the reversed flow grows upstream from the RC outlet position, which leads to the backflow ahead of the blade leading edge. It seems that the reversed flow area developed upstream of the RC outlet is not suppressed sufficiently even if the injection from the RC is strengthened. This may be the reason why any further improvement in the compressor rotor stall margin from Case #3 is not obtained in Case #4 and Case #5.

## 7.0 CONCLUSION

Steady and time-dependent Computational Fluid Dynamics have provided a useful insight into the flow regimes that characterise incipient tip stall in a highly loaded axial rotor, which may well represent an operating scenario of the engine axial compressor of a future combat air system. The benchmark case used is the NASA rotor 37, which is an established benchmark case of the turbomachinery research community. The NASA rotor 37 is a highly loaded axial rotor with a known propensity for tip stall and, as such, it was a good fit to this research.

It was found that, in this highly loaded axial rotor, the leakage flow at the rotor tip is not only responsible for a reduction in performance in terms of efficiency but also limits the operating range of the rotor. Once the leakage flow starts interacting with the neighbouring blade, it creates the conditions for the rotor to stall at the blade tip.

Computational Fluid Dynamics was then used to assess numerically a tip stall mitigation concept based on a recirculation channel in the casing. The new casing treatment design uses the pressure difference to activate the channel in the casing of the rotor. The channel is shaped in such a way to turn the flow towards the upstream axial direction. The outflow is directed as far as practicable against the oncoming spillage flow.

Numerical investigation of the channel parameter space, by varying the axial length, achieved a 9.11% improvement in the rotor stall margin with respect to the baseline CFD prediction, without any adiabatic efficiency penalty. Time-dependent RANS simulations provided some useful insights on the stall inception process in a highly loaded axial compressor with the recirculation channel treatment.

The next stage for the development of this new casing treatment involves laboratory scale testing on a rotational stage, followed by the implementation of the prototype on a test engine.

## ACKNOWLEDGEMENTS

The authors wish to acknowledge the insightful guidance on end-wall contouring design and axial compressor numerical modeling by Dr Tie Chen, Dr Christos Georgakis, and Mr Peter Millington, GE Power, Rugby, UK. Kawase's Ph.D. is supported by the Japanese Acquisition Technology & Logistic Agency, Government of Japan. This research used the ALICE high-performance computing facility at the University of Leicester. Graphical rendering software licenses were originally acquired with EPSRC support on Grant GR/N23745/01.

## REFERENCES

1. CAMP, T. R., and DAY, I. J., "A study of spike and modal stall phenomena in a low-speed axial compressor," *Journal of Turbomachinery*, **120**(3), 1997, pp. 393-401.
2. GALLIMORE, S. J., BOLGER, J. J., CUMPSTY, N. A., Taylor, M. J., Wright, P. I. and Place, J. M. M., "The use of sweep and dihedral in multistage axial flow compressor blading – Part 1: University research and methods development," *Journal of Turbomachinery*, **124**(4), 2002, pp. 521-532.
3. GALLIMORE, S. J., BOLGER, J. J., CUMPSTY, N. A., Taylor, M. J., Wright, P. I. and Place, J. M. M., "The use of sweep and dihedral in multistage axial flow compressor blading – Part 2: Low and high-speed designs and test verification," *Journal of Turbomachinery*, **124**(4), 2002, pp. 533-541.
4. VO, H. D., "Rotating stall suppression in axial compressors with casing plasma actuation," *Journal of Propulsion and Power*, **26**(4), 2010, pp. 808-818.
5. OSBORN, M. W., LEWIS, W. G. Jr., and HEIDELBERG, J. L., "Effect of several porous casing treatments on stall limit and on overall performance of an axial-flow compressor rotor," NASA Technical note TN D-6537, 1971.
6. SCHNELL, R., VOGES, M., MÖNIG, R., MÜLLER, M. W., and ZSCHNERP, C., "Investigation of blade tip interaction with casing treatment in a transonic compressor - Part 2: Numerical results," *Journal of Turbomachinery*, **133**(1), 2010, pp. 011008-1-11.
7. WADIA, A. R., and JAMES, F. D., "F110-GE-132: Enhanced power through low-risk derivative technology," *Journal of Turbomachinery*, **123**(3), 2000, pp. 544-551.
8. SAKUMA, Y., WATANABE, T., HIMENO, T., KATO, D., MUROOKA, T., and SHUTO, Y., "Numerical analysis of flow in a transonic compressor with a single circumferential casing groove: Influence of groove location and depth of flow instability," *Journal of Turbomachinery*, **136**(3), 2013, pp. 031017-1-9.
9. CEVIK, M., VO, H. D., and YU, H., "Casing treatment for desensitization of compressor performance and stability to tip clearance," *Journal of Turbomachinery*, **138**(12), 2016, pp. 121008-1-16.
10. KOFF, S. G., MAZZAWY, R. S., NIKKANEN, J. P., and NOLCHEFF, N. A., United Technology Corp., Hartford, CT, U. S. Patent application for a "Case treatment for compressor," 5282718, filed 3 August 1992.
11. HATHAWAY, M. D., "Self-recirculating casing treatment concept for enhanced compressor performance," NASA Technical memorandum TM-2002-211569, 2002.

12. DINH, C. T., MA, S. B., and KIM, K. Y., "Effect of a circumferential feed-back channel on aerodynamic performance of a single-stage transonic axial compressor," American Society of Mechanical Engineers, Paper GT2017-63536, 2017.
13. DUNHAM, J., "CFD validation for propulsion system components," AGARD-AR-355, May 1998.
14. SHIH, T. -H., LIOU, W. W., SHABBIR, A., YANG, Z. AND ZHU, J., "A new  $k-\varepsilon$  eddy-viscosity model for high Reynolds number turbulent flows- Model development and validation," Computers & Fluids, **24**(3), 1999, pp. 227-238.
15. VAN LEER, B., THOMAS, J. L., ROE, P. L. and NEWSOME, R. W., "A comparison of numerical flux formulas for the Euler and Navier-Stokes equations," 8th The American Institute of Aeronautics and Astronautics, computational Fluid dynamics conference, Technical report AIAA-87-1104, 1987.
16. WEISS, J. M., MARUSZEWSKI, J. P., and SMITH, W. A., "Implicit solution of the Navier-Stokes equations on unstructured meshes," The American Institute of Aeronautics and Astronautics, Technical report AIAA-97-2103, 1997.
17. PANDYA, S. A., VENKATESWARAN, S., and PULLIAM, T. H., "Implementation of dual-time procedures in overflow" 41st Aerospace Sciences Meeting and Exhibit, Aerospace sciences meeting, Technical report AIAA-2003-0072, 2003.
18. TURKEL, E., and VATSA, V. N., "Choice of variables and preconditioning for time dependent problems," 16th The American Institute of Aeronautics and Astronautics, Computational Fluid Dynamics conference, Technical Report AIAA-2003-3692, 2003.
19. MOORE, R. D. and REID, L., "Performance of single-stage axial flow transonic compressor with rotor and stator aspect ratios of 1.19 and 1.26, respectively, and with design pressure ratio of 2.05," NASA Technical paper TP 1659, 1980.
20. TSEDERBERG, N. V., 1965, *Thermal conductivity of gases and liquids*. London, UK: Edward Arnold.
21. OUTA, E., KATO, D., and CHIBA, K., " An N-S simulation of stall cell behaviour in a 2-D compressor rotor-stator system at various loads," American Society of Mechanical Engineers, Paper No. 94-GT-257, 1994.
22. ROACHE, P. J., "Perspective: A method for uniform reporting of grid refinement studies," Journal of Fluids Engineering, **116**(3), 1994, pp. 405-413.
23. ARIMA, T., SONODA, T., SHIOTORI, M., TAMURA, A., and KIKUCHI, K., "A numerical investigation of transonic axial compressor rotor flow using a low-Reynolds-number  $k-\varepsilon$  turbulence model," Journal of Turbomachinery, **121**(1), 1999, pp. 44-58.
24. CAMERON, J. D., MORRIS, S. C., BARROWS, S. T., and CHEN, J. P., "On the interpolation of casing measurements in axial compressors," American Society of Mechanical Engineers, Paper GT2008-51371, 2008.
25. HAH, C., "Large eddy simulation of transonic flow field in NASA rotor 37," NASA Technical memorandum NASA/TM-2009-215627, 2009.
26. KIM, D. -W., KIM, J. -H., and KIM, K. -Y., "Aerodynamic performance of an axial compressor with a casing groove combined with injection," Transactions of the Canadian Society for Mechanical Engineering, **37**(3), 2013, pp. 283-292.
27. ZHU, X., LIU, B., HU, J., and SHEN, X., "Numerical study of stall inception in a transonic axial compressor rotor based on the throttle model," Journal of Theoretical and Applied Mechanics, **53**(2), 2015, pp. 307-316.
28. VO, H. D., TAN, C. S., and GREITZER, D. M., "Criteria for spike initiated rotating stall," Journal of Turbomachinery, **130**(1), 2008, pp. 011023-1-9.
29. TESLA, N., New York, NY, U. S. Patent Application for a "Valvular Conduit," 1329559, filed 2 February 1916.
30. CUMPSTY, N. A., 1989, *Compressor aerodynamics*. Essex, UK: Longman Scientific & Technical, Longman Group UK Ltd.